

# A Room-Temperature Postsynthetic Ligand Exchange Strategy to Construct Mesoporous Fe-Doped CoP Hollow Triangle Plate Arrays for Efficient Electrocatalytic Water Splitting

Enlai Hu, Jiqiang Ning, Dian Zhao, Chunyang Xu, Yingying Lin, Yijun Zhong, Ziyang Zhang, Yongjiang Wang, and Yong Hu\*

Hollow nanostructures with mesoporous shells are attractive for their advantageous structure-dependent high-efficiency electrochemical catalytic performances. In this work, a novel nanostructure of Fe-doped CoP hollow triangle plate arrays (Fe–CoP HTPAs) with unique mesoporous shells is designed and synthesized through a room-temperature postsynthetic ligand exchange reaction followed by a facile phosphorization treatment. The mild postsynthetic ligand exchange reaction of the presynthesized ZIF-67 TPAs with  $K_4[Fe(CN)_6]$  in an aqueous solution at room temperature is of critical importance in achieving the final hollow nanostructure, which results in the production of CoFe(II)-PBA HTPAs that not only determine the formation of the interior voids in the nanostructure, but also provide the doping of Fe atoms to the CoP lattice. As expected, the as-prepared mesoporous Fe–CoP HTPAs exhibit pronounced activity for water splitting owing to the advantages of abundant active reaction sites, short electron and ion pathways, and favorable hydrogen adsorption free energy ( $\Delta G_{H^*}$ ). For the hydrogen and oxygen evolution reactions with the Fe–CoP HTPAs in alkaline medium, the low overpotentials of 98 and 230 mV are observed, respectively, and the required cell voltage toward overall water splitting is only as low as 1.59 V for the driving current density of  $10 \text{ mA cm}^{-2}$ .

metal compounds, transition metal-based phosphides (TMPs) have been identified as high activity and stability electrocatalysts for water splitting.<sup>[11–15]</sup> Although the intrinsic structure of TMPs makes them outstanding electrocatalysts, further promotion of their water splitting performance is still desired. On the one hand, the element doping or alloying has been illustrated to be a favorable approach to further improve the intrinsic activities of monophase TMPs toward HER and OER by means of tuning electronic structures and optimizing the intermediates absorption energy.<sup>[8,16–20]</sup> On the other hand, hollow nanostructures composed of mesoporous shells have also been explored due to their unique structure-dependent properties such as large exposed surface with abundant accessible active sites and short diffusion pathway for catalyst reactions.<sup>[21–23]</sup> Till now, although there are some research works on Fe-doped CoP (Fe–CoP) electrocatalysts for HER or OER,<sup>[24,25]</sup> their applications for overall

water splitting are still rare. In particular, Fe–CoP catalysts with well-defined mesoporous shells are not reported yet.

Metal-organic frameworks (MOFs) have been widely utilized as the templates to construct hollow or porous structures for the achievement of superior thermal property and chemical reactivity.<sup>[26,27]</sup> Lou and co-workers have constructed a series of nanostructures such as  $MoC_x$  nanooctahedrons, cobalt-based complex hollow nanostructure, and iron-based hierarchical microboxes from a variety of MOF precursors.<sup>[28–30]</sup> Besides the direct strategy of transforming MOFs into the final products, the MOF technique can be further expanded by transferring

## 1. Introduction

Electrochemical water splitting, involving two half reactions of oxygen evolution reaction (OER) and hydrogen evolution reaction (HER), has been widely explored as a promising approach to obtain clean renewable energy.<sup>[1,2]</sup> To cut the use of noble-metal-based electrocatalysts such as  $IrO_2/RuO_2$  for OER and Pt for HER,<sup>[3–5]</sup> enormous efforts have been afforded to expedite the thermodynamically unfavorable procedure of OER and HER at low overpotentials by using cost-efficient and earth-abundant electrocatalysts.<sup>[6–10]</sup> As one type of non-noble

E. Hu, Prof. D. Zhao, C. Xu, Y. Lin, Prof. Y. Zhong, Prof. Y. Hu  
Key Laboratory of the Ministry of Education  
for Advanced Catalysis Materials  
Department of Chemistry  
Zhejiang Normal University  
Jinhua 321004, China  
E-mail: yonghu@zjnu.edu.cn, yonghuzjnu@163.com

Dr. J. Ning, Prof. Z. Zhang, Prof. Y. Wang  
Vacuum Interconnected Nanotech Workstation  
Suzhou Institute of Nano-Tech and Nano-Bionics  
Chinese Academy of Sciences  
Suzhou 215123, China  
Prof. Y. Zhong, Prof. Y. Hu  
Hangzhou Institute of Advanced Studies  
Zhejiang Normal University  
Hangzhou 311231, China

 The ORCID identification number(s) for the author(s) of this article can be found under <https://doi.org/10.1002/smll.201704233>.

DOI: 10.1002/smll.201704233

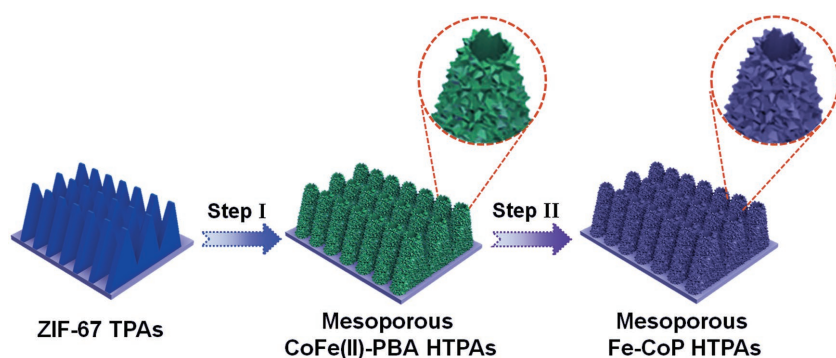


**Figure 1.** Schematic illustration of the construction of mesoporous Fe–CoP HTPAs.

one kind of MOF into another kind through postsynthetic means such as ligand exchange reactions and cation exchange reactions.<sup>[31]</sup> However, these two methods are limited by their technique issues, including complex and time-consuming heating procedures as well as the indispensable utilization of toxic organic solvents (such as methanol or dimethyl formamide) in some cases.<sup>[32]</sup> It is therefore highly desirable to develop mild time and energy saving approaches to achieve the MOF-to-MOF transformation.

In this work, we present a novel MOF-to-MOF strategy to synthesize mesoporous Fe–CoP hollow triangular plate arrays (Fe–CoP HTPAs) by using the monometallic Co-based zeolitic imidazolate framework (ZIF-67) through a room-temperature postsynthetic ligand exchange reaction followed by a facile phosphorization treatment. In this strategy, the critical postsynthetic ligand exchange reaction of 2-methylimidazole (MIM) with  $K_4[Fe(CN)_6]$  occurred within several hours at room temperature in an aqueous solution, which constructs the hollow array structures and provides the doping source of Fe atoms for the final mesoporous product. The as-prepared mesoporous Fe–CoP HTPAs are featured with a variety of favorable characteristics for water splitting, including the synergetic bimetal composition, abundant active sites, short electron and ion transport pathways, high structural strength, and thus pronounced electrocatalytic performance and long durability toward both HER and OER are obtained due to the advantageous interior voids in the mesoporous shells. Remarkably, the overpotential of 98 mV for HER and 230 mV for OER at  $10\text{ mA cm}^{-2}$  were obtained with the mesoporous Fe–CoP HTPAs, which are 22 and 40 mV lower than those of nondoped CoP TPAs, respectively. Moreover, employing the as-prepared electrocatalysts as both the cathode and the anode, the assembled alkaline electrolyzer worked for overall water splitting and displayed a low cell potential of 1.59 V at the current density of  $10\text{ mA cm}^{-2}$ , as compared with as the value of 1.65 V for CoP TPAs.

## 2. Results and Discussion

The synthetic procedure of the mesoporous Fe–CoP HTPAs is schematically illustrated in **Figure 1**. First, ZIF-67 TPAs are directly grown on the surface of nickel foam (NF) via a facile reaction of  $Co(NO_3)_2$  with MIM in an aqueous solution, which

takes place at room temperature in 2 h.<sup>[33]</sup> In step I, the as-obtained ZIF-67 TPAs are then immersed into the  $K_4[Fe(CN)_6]$  aqueous solution at room temperature and maintained for 8 h to allow the mild postsynthetic ligand exchange reaction to produce the mesoporous prussian blue analogue  $Co_2[Fe(CN)_6]$  (CoFe(II)-PBA) HTPAs. In step II, by using  $NaH_2PO_2$  as the phosphorus source, the CoFe(II)-PBA HTPAs are phosphorized through a 2 h reaction in  $N_2$  atmosphere at  $300\text{ }^\circ\text{C}$ , and the final product of the mesoporous Fe–CoP HTPAs are obtained.

The as-prepared ZIF-67 TPAs are first characterized by the technique of powder X-ray diffraction (XRD) to examine the crystallographic structure and phase purity. As shown in Figure S1 in the Supporting Information, except the three strong peaks assigned to NF, all the peaks can be indexed to ZIF-67 as reported.<sup>[33]</sup> The panoramic scanning electron microscopy (SEM) image presented in Figure S2a,b in the Supporting Information reveals that the ZIF-67 TPAs are vertical aligned on NF. The magnified SEM image in Figure S2b in the Supporting Information further indicates that the as-obtained ZIF-67 TPAs exhibit a smooth surface, an average thickness of 300 nm and an average length of several micrometers. After the room-temperature postsynthetic ligand exchange reaction, the ZIF-67 TPAs were converted into mesoporous CoFe(II)-PBA HTPAs, with a rough surface with hollow interiors created and the triangular shape and vertical aligned structural units well maintained (see Figure S2c,d in the Supporting Information). Furthermore, Figure S2d and the inset in Figure S2d in the Supporting Information reveal open voids in some triangular plates, indicating the obvious hollow and porous nature of the structure. The evolution of internal void might be a result of the diffusion of different ligand species, similar to the diffusion of cationic and anionic species in an ion exchange reaction.<sup>[34]</sup> In the ligand exchange reaction, the smaller ligands may diffuse outward from the pristine ZIF-67 triangular plate, leading to a steady growth of the CoFe(II)-PBA shells over the whole triangular plate. Consequently, mesoporous CoFe(II)-PBA HTPAs with well-defined hollow interiors are formed. The successful formation of CoFe(II)-PBA HTPAs can be further confirmed by the XRD results. As shown in Figure S1 in the Supporting Information, the diffraction pattern clearly confirms that the ZIF-67 TPAs are converted into CoFe(II)-PBA HTPAs ( $Co_2[Fe(CN)_6]$ , JCPDS card No. 79-0039), and the weak diffraction peaks mainly result from the poor crystallinity or small crystal domain in the as-prepared sample.<sup>[35]</sup> The chemical structure of the ZIF-67 TPAs and the CoFe(II)-PBA HTPAs are further examined by the Fourier transform-infrared spectroscopy. As shown in Figure S3 in the Supporting Information, after the postsynthetic ligand exchange reaction, all the characteristic absorption peaks for ZIF-67 TPAs, such as  $1143\text{ cm}^{-1}$  and  $1305\text{ cm}^{-1}$  for C–H vibrations  $1384\text{ cm}^{-1}$  for C–C stretching and  $1566\text{ cm}^{-1}$  for C=N stretching disappear,<sup>[36]</sup> and the characteristic peaks for CoFe(II)-PBA HTPAs, including  $458\text{ cm}^{-1}$  for Fe–CN vibration,  $596\text{ cm}^{-1}$  for Fe–C vibration and  $2080\text{ cm}^{-1}$  for C≡N stretching,<sup>[37]</sup> get remarkably detectable. This result

further confirms the successful transformation of ZIF-67 TPAs to CoFe(II)-PBA HTPAs. Moreover, only CoP TPAs can be obtained without the postsynthetic ligand exchange reaction (Figure S4, Supporting Information), indicating that the postsynthetic ligand exchange reaction is crucial for the construction of the hollow arrays.

The mesoporous CoFe(II)-PBA HTPAs can be transformed into mesoporous Fe–CoP HTPAs through a facile phosphorization treatment. As confirmed by the XRD pattern in Figure S5 in the Supporting Information, the diffraction peaks of Fe–CoP HTPAs can be attributed to the characteristics of orthorhombic CoP (JCPDS card No. 65–2593,  $a = 5.076 \text{ \AA}$ ,  $b = 3.277 \text{ \AA}$ ,  $c = 5.599 \text{ \AA}$ ), without any impurity phase of iron phosphide in the final sample, which implies that the Fe dopant was achieved.<sup>[20]</sup> Moreover, the energy dispersive X-ray spectrum (Figure S6, Supporting Information) of the mesoporous Fe–CoP HTPAs displays the presence of Fe, Co, and P elements, which further confirms the successful formation of Fe–CoP HTPAs. Revealed by the SEM images in Figure 2a,b, the hollow and porous structure and the vertically aligned structural units are well inherited from the CoFe(II)-PBA HTPAs. The magnified SEM image (the inset in Figure 2b) clearly shows the open void of the Fe–CoP HTPAs. To further confirm the hollow structure of the as-prepared, focused ion beam scanning electron microscopy (FIB-SEM) was conducted. As shown in Figure 2c,d, the Fe–CoP TPAs milled by FIB using gallium ion beam clearly present a totally different frame, from which uniform hollow interior can be observed in all of the as-prepared Fe–CoP TPAs. The detailed geometrical structure of the

as-obtained mesoporous Fe–CoP HTPAs are further uncovered by the transmission electron microscopy (TEM) measurements (Figure 3a,b). The magnified TEM image (Figure 3b) clearly shows that the shell of the mesoporous Fe–CoP HTPAs is composed of many interconnected nanoparticles with a large amount of mesopores distributed. As demonstrated by the distinct hysteresis loop in the  $N_2$  sorption adsorption–desorption isotherm (Figure S7a, Supporting Information), the Fe–CoP HTPAs exhibit a mesoporous feature with a relatively high Brunauer–Emmett–Teller (BET) surface area of  $22.03 \text{ m}^2 \text{ g}^{-1}$  and the main pore size of  $2.48 \text{ nm}$ ,<sup>[38]</sup> while the BET surface area of the CoP TPAs is examined to be  $17.62 \text{ m}^2 \text{ g}^{-1}$  and the pore size is  $5.59 \text{ nm}$  (Figure S7b, Supporting Information). Such hollow and mesoporous structural nature of the Fe–CoP HTPAs holds great promise in delivering plenty of active sites and facilitating the transport of active species to boost electrochemical reactions.<sup>[22]</sup> High resolution TEM (HRTEM) image (Figure 3c) of the mesoporous Fe–CoP HTPAs displays an interplanar spacing of  $0.25 \text{ nm}$ , which is consistent with the lattice distance of the CoP (200) plane. Moreover, the selected-area diffraction (SAED) pattern for hierarchical mesoporous Fe–CoP HTPAs (Figure 3d) can be well indexed into (011), (200), (211), and (301) plans of CoP, corresponding to the XRD result, which indicates that the obtained sample is a ternary compound of Fe–Co–P rather than a mixture of two metal phosphides. The chemical composition and element distribution of the mesoporous Fe–CoP HTPAs are further illustrated by the elemental mapping measurements. As shown in Figure 3e–h, the Co, Fe, and P elements are uniformly distributed

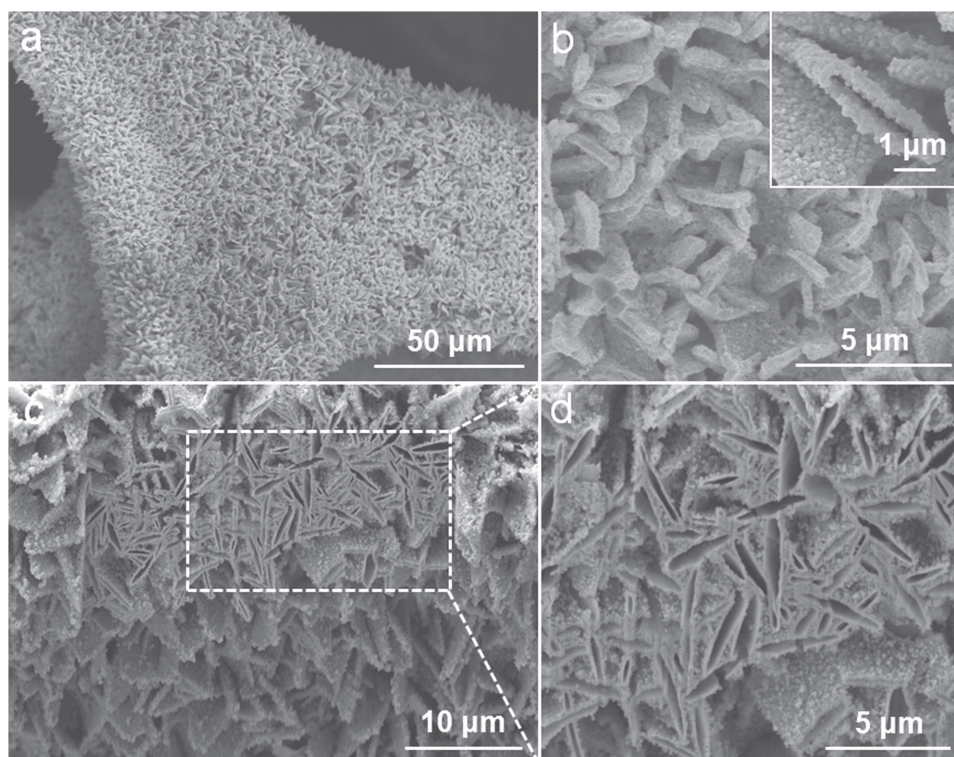


**Figure 2.** a,b) SEM, c,d) FIB-SEM images of the as-prepared mesoporous Fe–CoP HTPAs. The inset in (b) shows a magnified SEM image of Fe–CoP HTPAs.

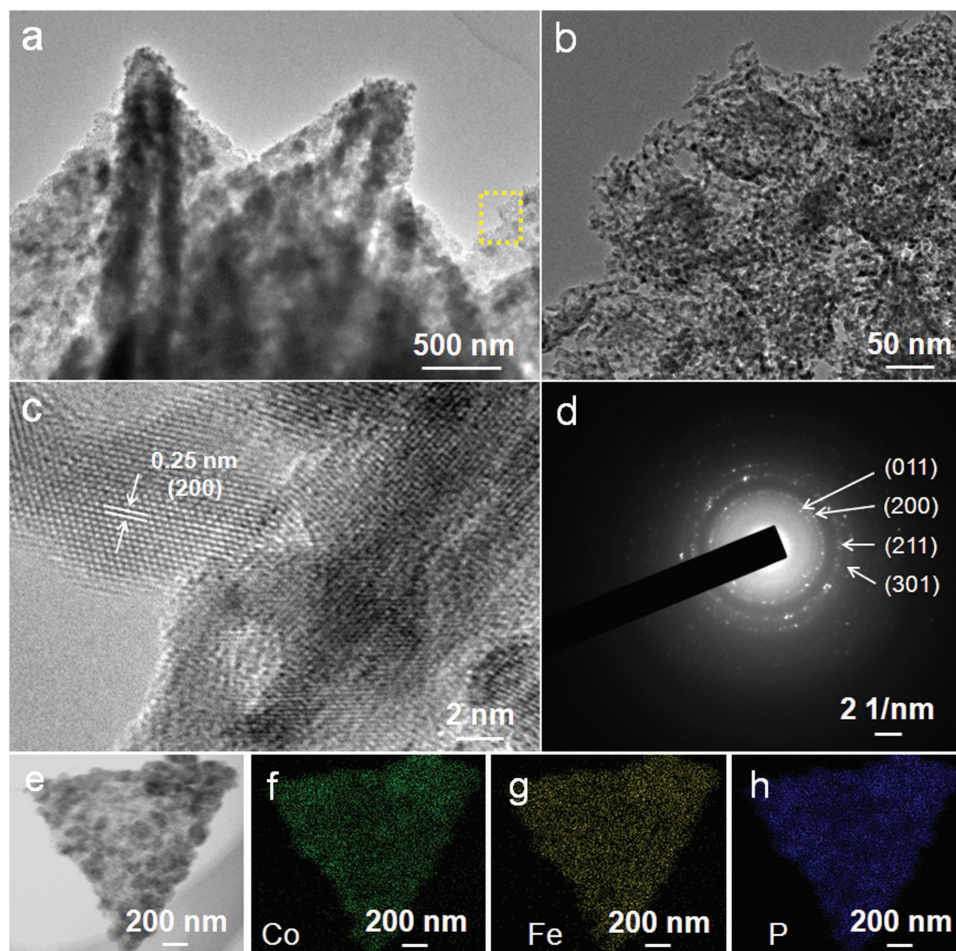


**Figure 3.** a,b) TEM, c) HRTEM, d) corresponding SAED pattern, and e) STEM images of the as-prepared mesoporous Fe–CoP HTPAs, and elemental mapping images of f) Co, g) Fe, and h) P.

throughout the whole triangular plate. All the above results provide solid evidences to demonstrate the successful formation of mesoporous Fe–CoP TPAs.

The X-ray photoelectron spectroscopy (XPS) results are also employed to further elucidate the surface chemical composition and chemical states in the mesoporous Fe–CoP HTPAs. As shown in Figure 4a, the XPS spectrum of the as-prepared sample reveals the existence of Co, Fe, and P elements as well as C and O elements which may arise from the contamination and superficial oxidation of the sample in the air contact.<sup>[39]</sup> The high-resolution XPS spectra of Co 2p (Figure 4b) exhibits two spin-orbit doublets corresponding to the shakeup satellites (identified as “Sat.”). One of the spin-orbit doublet located at 778.6 and 793.6 eV can be indexed to the Co species in Fe–CoP.<sup>[8,24]</sup> The other spin-orbit doublet at 781.5 and 797.5 eV corresponds to oxidized Co species which arose from the superficial oxidation.<sup>[40]</sup> The high-resolution XPS spectrum of Fe 2p (Figure 4c) is deconvoluted into a spin-orbit doublet at 707.2 and 720.4 eV, which can be assigned to the binding energies for Fe species in Fe–CoP.<sup>[20,41]</sup> The broad peak centered at 712.9 eV is attributed to the Fe oxidation state resulting from the surface oxidation, which is consistent with previous work,<sup>[20]</sup> with a satellite peak located at about 718.2 eV.<sup>[42,43]</sup> The P 2p core level

spectrum (Figure 4d) reveals three main peaks at 129.3, 130.1, and 133.7 eV. The former two peaks are the characteristic of low-valence P species in Fe–CoP and the latter can be assigned to the oxidized P species which were produced by the surface oxidation due to the exposure to air.<sup>[20]</sup>

The void interiors, mesoporous shells, and vertically aligned structural units are expected to endow the Fe–CoP HTPAs with improved electrocatalytic activity. The water splitting activities of the as-prepared Fe–CoP HTPAs catalyst were first examined for HER in an alkaline solution (1 M KOH), with a conventional electrochemical three-electrode cell measured with a scan rate of 5 mV s<sup>-1</sup>. As shown by the iR-corrected polarization curves in Figure 5a, the mesoporous Fe–CoP HTPAs exhibit superior HER performance to CoP TPAs. To drive a current density of 10 mA cm<sup>-2</sup>, the mesoporous Fe–CoP HTPAs require an overpotential of 98 mV, while the overpotential for CoP TPAs is high up to 120 mV. Furthermore, the HER performance of NF substrate is also evaluated, and the activity is inferior to that of Fe–CoP HTPAs (Figure S8a, Supporting Information). The HER performance of the mesoporous Fe–CoP HTPAs is compared in Table S1 in the Supporting Information with other reported representative HER electrocatalysts including CoS<sub>2</sub> nanotube arrays (193 mV) and MoS<sub>2</sub>/Ni<sub>3</sub>S<sub>2</sub>

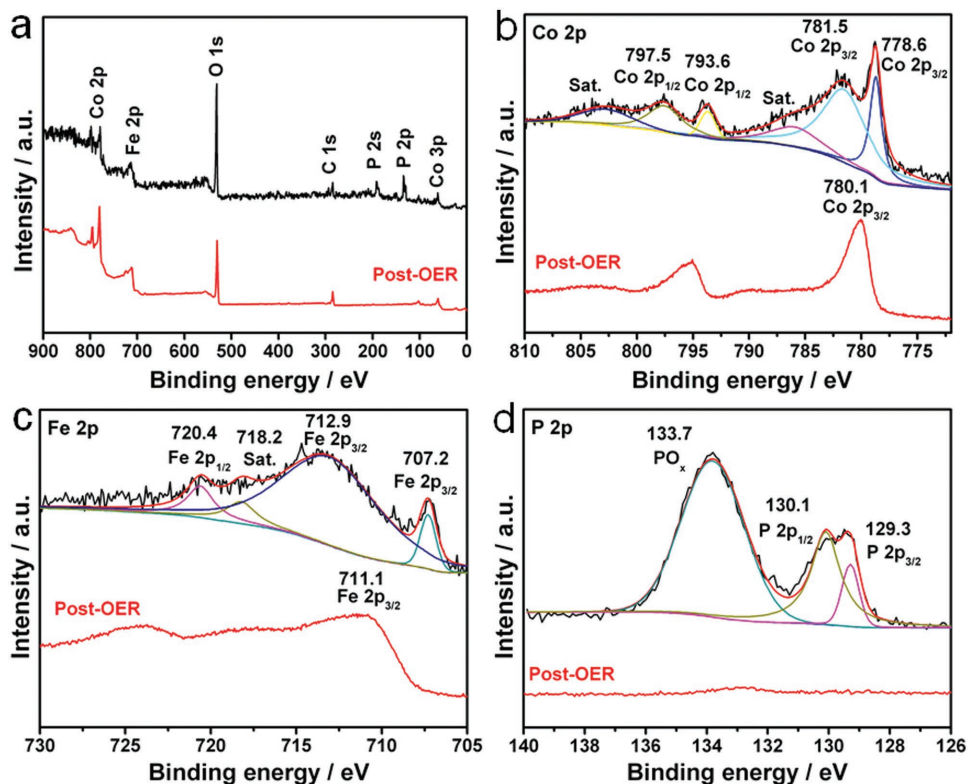


**Figure 4.** a) XPS survey spectrum and high-resolution XPS spectra of b) Co 2p, c) Fe 2p, and d) P 2p of the Fe–CoP HTPAs before and after OER performance.

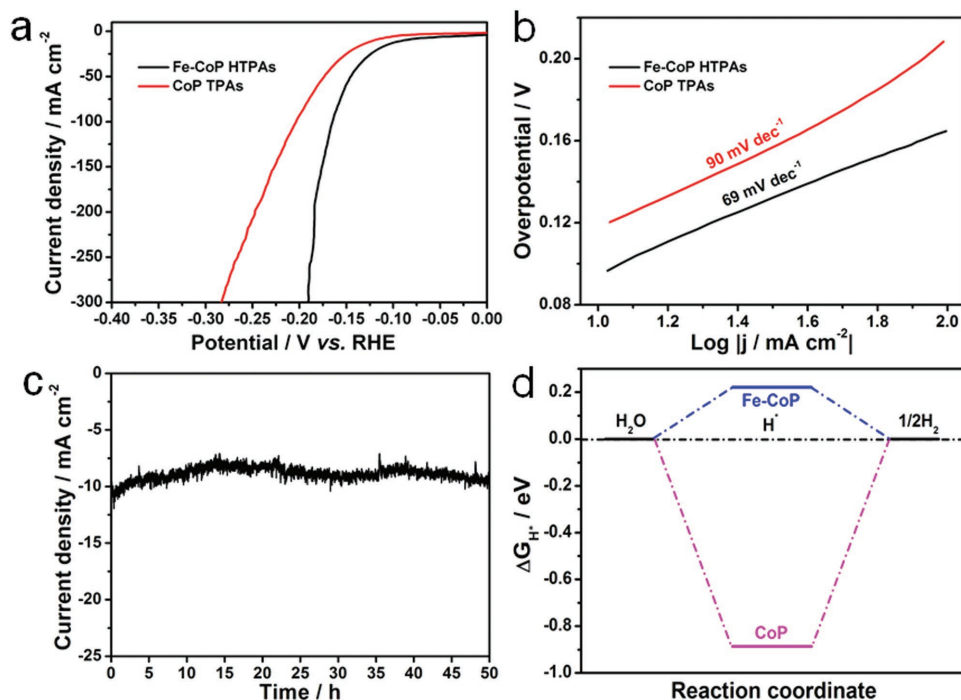


**Figure 5.** a) Polarization curves obtained in 1 M KOH solution with a scan rate of 5 mV s<sup>-1</sup> at room temperature and b) Tafel plots of the as-prepared mesoporous Fe–CoP HTPAs and CoP TPAs for HER. c) Chronoamperometry curve of the mesoporous Fe–CoP HTPAs for HER obtained at –0.098 V versus RHE at room temperature. d) Calculated free-energy changes for Fe–CoP and CoP.

(110 mV).<sup>[44,45]</sup> To have further insight into the performance of the as-obtained products, the Tafel slopes of the two samples were also evaluated. As shown in Figure 5b, the Tafel slope for the mesoporous Fe–CoP HTPAs is measured as 69 mV dec<sup>-1</sup>, much smaller than 90 mV dec<sup>-1</sup> of CoP TPAs, suggesting a more favorable HER rate achieved by using the mesoporous Fe–CoP HTPAs.

Cyclic voltammetry measurements were also conducted to determine the value of double-layer capacitances ( $C_{dl}$ ). Obtained from the results shown in Figure S9 in the Supporting Information, the mesoporous Fe–CoP HTPAs exhibit a much higher  $C_{dl}$  of 127.9 mF cm<sup>-2</sup>, which is nearly 2.9 times that of CoP TPAs (43.7 mF cm<sup>-2</sup>), indicating the much higher HER activity. Since the double-layer capacitance  $C_{dl}$  is linearly proportional to the electrochemically active surface area,<sup>[8]</sup> the high value of  $C_{dl}$  could rise from the hollow and porous structural nature and the considerable exposed active sites. To investigate the charge-transfer kinetics, electrochemical impedance spectroscopy (EIS) measurements were performed. The Nyquist impedance plots in Figure S10a in the Supporting Information are fitted to an equivalent electronic circuit, which includes a series solution-spreading resistance ( $R_s$ ), a charge-transfer resistance ( $R_{ct}$ ) in parallel with a constant phase-element (CPE). As compared with CoP TPAs, a smaller  $R_{ct}$  and larger CPE-T listed in Figure S10b in the Supporting Information can be observed with the mesoporous Fe–CoP HTPAs, which can be another reason for the improved HER performance of the Fe–CoP HTPAs.<sup>[46]</sup> The chronoamperometric response at the fixed overpotential of 98 mV reveals the high stability of the mesoporous Fe–CoP HTPAs. Remarkably, as shown in Figure 5c, the current density is negligibly declined over 50 h, indicating the apparent advantage of mesoporous Fe–CoP HTPAs as a high-performance HER electrocatalyst.

To understand the influence of the doped Fe atoms on the electrocatalytic HER performance, density functional theory (DFT) calculation was utilized to investigate the water adsorption energy ( $\Delta G_{H_2O^*}$ ) and  $\Delta G_{H^*}$  in an alkaline medium. The adsorption sites of H atoms were selected as Co–Co bridge sites in the calculations (Figure S11, Supporting Information). It has been reported that an optimal HER electrocatalyst should have an appropriate  $\Delta G_{H^*}$  close to zero.<sup>[24]</sup> Figure 5d compares the  $\Delta G_{H^*}$  diagrams of the Fe–CoP HTPAs and CoP TPAs electrocatalysts. Obviously, with Fe doped into the CoP lattice, the  $\Delta G_{H^*}$  of Fe–CoP HTPAs is found to be more close to the optimal  $\Delta G_{H^*}$  of zero, indicating the state of catalyst-H\* is more favorable on the surface of the Fe–CoP HTPAs during the HER process.<sup>[9]</sup> Additionally, according to the similar  $\Delta G_{H_2O^*}$  for the Fe–CoP HTPAs (–0.7 eV) and CoP TPAs (–1.1 eV) shown in Figure S12 in the Supporting Information, we can see that the doped Fe atoms have limited influence on the ability of water adsorption. As a result, the determinant process for the enhanced HER activity is the H adsorption at the surface of the catalyst, in other words, the doped Fe atoms have a significant and positive influence on the H adsorption energy, resulting in the improved HER activity. As reported by previous theoretical calculations and experiment examination, the Co or Fe atoms in the phosphides carry partially positive charges ( $\delta^+$ ), while P atoms possess partially negative charge ( $\delta^-$ ).<sup>[20]</sup> Due to the lower electron negativity of Fe atom than that of Co atom, a weakened

strength of hydrogen on Co sites would be achieved.<sup>[24]</sup> As a result, Fe–CoP HTPAs is found to be more close to the optimal  $\Delta G_{H^*}$  of zero.

The OER performances of the mesoporous Fe–CoP HTPAs and CoP TPAs were also evaluated by using an electrochemical three-electrode cell with an alkaline solution (1 M KOH) and measuring with a scan rate of 1 mV s<sup>-1</sup>. The polarization curves with iR correction of the as-prepared samples are presented in Figure 6a. The overpotential of CoP TPAs is determined to be 270 mV at the current density of 10 mA cm<sup>-2</sup>. With the incorporation of Fe atoms, the OER activity of the Fe–CoP HTPAs is greatly enhanced, manifested as the overpotential of 230 mV at the same current density of 10 mA cm<sup>-2</sup>, which is 40 mV less than that of CoP TPAs. The mesoporous Fe–CoP HTPA catalyst shows comparable or even superior performance to many other state-of-the-art nonprecious-metal electrocatalysts (Table S2, Supporting Information), such as NiCoP/NF (280 mV),<sup>[8]</sup> and CoFeNiO<sub>x</sub> (240 mV).<sup>[47]</sup> The Tafel plots of the samples are shown in the inset of Figure 6a. Compared with the value of 82 mV dec<sup>-1</sup> for CoP TPAs, the mesoporous Fe–CoP HTPAs exhibit a much lower Tafel slope of 43 mV dec<sup>-1</sup>, indicating the favorable reaction kinetics of the Fe–CoP HTPA catalyst toward OER. Furthermore, the OER performance of NF substrate is also evaluated, and the activity is inferior to that of Fe–CoP HTPAs (Figure S8b, Supporting Information). Through the rotating ring disk electrode setting according to the previous papers,<sup>[6,48]</sup> the Faradaic efficiency of the OER process occurring on the Fe–CoP HTPAs is determined to be about 96.1% (Figure S13, Supporting Information). The long-term stability of the mesoporous Fe–CoP HTPAs was examined by chronoamperometry at the fixed overpotential of 230 mV (Figure 6b). Remarkably, the change of the current density is negligible over 50 h, indicating the high catalytic stability in the alkaline condition. Moreover, EIS measurements were carried out to investigate the interfacial properties of the as-prepared electrodes. As can be seen in Figure S10c in the Supporting Information, the Nyquist impedance plots are fitted to an equivalent electronic circuit including  $R_s$ ,  $R_{ct}$ , and CPE. In Figure S10d in the Supporting Information, the mesoporous Fe–CoP HTPAs show a smaller  $R_{ct}$  than that of CoP TPAs, revealing a fast charge-transfer rate, which might account for the pronounced OER performance of the Fe–CoP HTPAs.<sup>[49]</sup> In addition, we further conducted XRD, XPS, and TEM measurements to characterize the sample after the OER performance. As shown in XRD pattern (Figure S14, Supporting Information), the peaks of CoP are missing, while some new weak and asymmetric peaks attributed to the CoOOH appeared after the OER test, which plays a vital role in the OER performance. Furthermore, XPS characterization was also used to determine the surface composition and chemical states of the electrocatalyst after OER. As shown in Figure 4a red curve, the sample after OER test still exhibits Co, Fe elements, but the P element is missing, indicating the P atoms are etching away during the OER test. And the Co 2p<sub>3/2</sub> spectrum (Figure 4b, red curve) with a predominate peak located at 780.1 eV can be indexed to the Co species in CoOOH.<sup>[50]</sup> The Fe 2p<sub>3/2</sub> spectrum (Figure 4c, red curve) with a broad peak centered at about 711.1 eV can be assigned to Fe species in FeOOH.<sup>[51]</sup> Furthermore, the HRTEM image in Figure S15 in the Supporting Information shows that

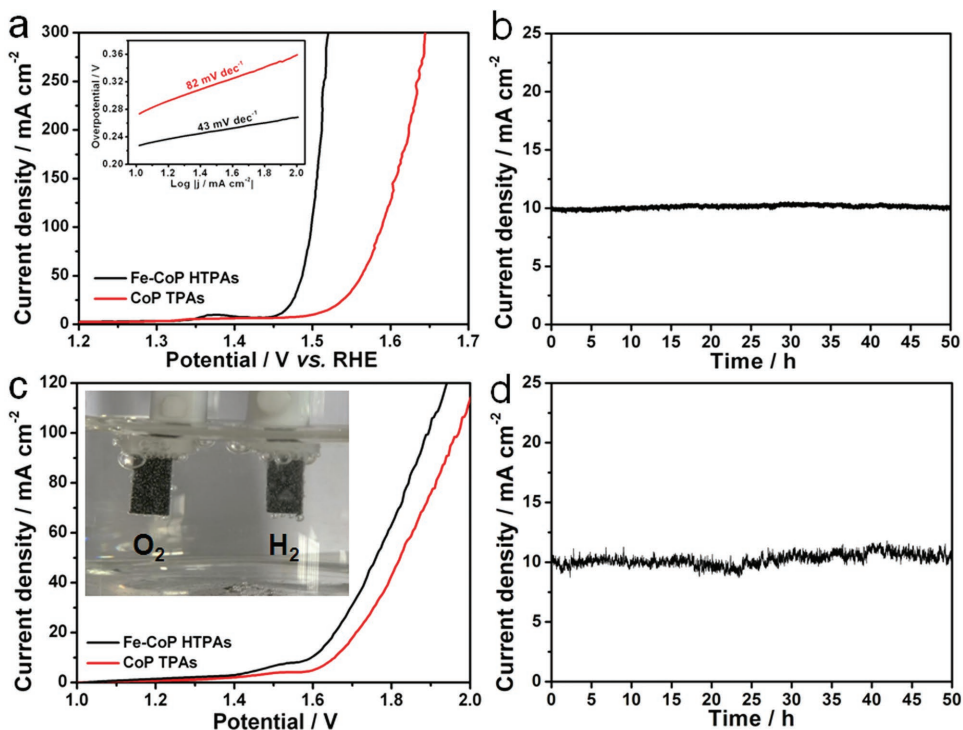


**Figure 6.** a) Polarization curves of the as-prepared mesoporous Fe–CoP HTPAs and CoP TPAs for OER obtained in 1 M KOH solution with a scan rate of  $1 \text{ mV s}^{-1}$  at room temperature. b) Chronoamperometry curve of Fe–CoP HTPAs for OER obtained at 1.46 V versus RHE at room temperature. The inset in (a) is the corresponding Tafel plots. c) Polarization curves of Fe–CoP HTPAs and CoP TPAs for overall water splitting obtained in 1 M KOH solution with a scan rate of  $1 \text{ mV s}^{-1}$  at room temperature. d) Chronoamperometry curve of Fe–CoP HTPAs for overall water splitting obtained at 1.59 V at room temperature. The inset in (c) shows a snap of overall water splitting experiment.

some oxidation species are formed. The lattice spacing  $d$  of 0.25 nm can be determined to the (100) plane of  $\text{CoOOH}$ . The above results suggest that the metal phosphide is being oxidized to metal oxyhydroxides, the real active materials for catalyzing OER, which is commonly observed in the previous work.<sup>[8,20]</sup> Generally, the enhanced electrocatalytic activity of the Fe–CoP HTPAs can be attributed to the hollow and mesoporous structure as well as the synergistic effect between the two metal centers. The porous structure can create abundant active sites to facilitate the electrocatalytic process, and the hollow structure with high specific surface area endows the catalyst with facile diffusion of the active species. Moreover, the synergistic interaction of Co and Fe is expected to have a positive effect on decreasing the adsorption energies of some catalytic species and therefore increase the OER activity.<sup>[52,53]</sup> In the OER progress, the real active species are expected to be  $\text{Co}_{1-x}\text{Fe}_x\text{OOH}$  derived from the Fe–CoP HTPAs. Recent works have demonstrated that Fe in  $\text{Co}_{1-x}\text{Fe}_x\text{OOH}$  is the most-active site, while  $\text{CoOOH}$  is expected to be a conductive and chemically stabilizing host.<sup>[50,54]</sup> Therefore, the incorporation of Fe will provide more Fe sites for promoting OER performance.

Inspired by the outstanding electrocatalytic performance of the mesoporous Fe–CoP HTPAs toward both HER and OER, we further examine its potential for overall water splitting by utilizing the Fe–CoP catalyst as both the anode and the cathode in a two-electrode cell. The polarization curves for overall water splitting obtained in 1 M KOH with a scan rate of  $1 \text{ mV s}^{-1}$  are shown in Figure 6c. As we can see, only a low cell voltage of

1.59 V is required for the Fe–CoP HTPAs to achieve the current density of  $10 \text{ mA cm}^{-2}$ . In contrast, the overall water splitting activity of the CoP sample without Fe doping is inferior to the doped one, requiring a cell voltage of 1.65 V to drive the current density to  $10 \text{ mA cm}^{-2}$ . Additionally, it was very evident to catch sight of the evolution of hydrogen and oxygen from the anode and cathode (inset in Figure 6c), respectively. The cell voltage of the Fe–CoP HTPAs is comparable to many recently reported earth-abundant electrocatalysts for overall water splitting (see Table S3 in the Supporting Information). The chronopotentiometry result of the Fe–CoP HTPAs is shown in Figure 6d, which indicates the very stable current density over 50 h. The low cell voltage and long-term durability of the Fe–CoP HTPAs demonstrate their promising practical applications for overall water splitting.

### 3. Conclusions

In summary, we have developed a facile room-temperature strategy to synthesize mesoporous Fe–CoP HTPAs, which involves a mild postsynthetic ligand exchange reaction followed by a simple phosphorization treatment. The postsynthetic ligand exchange method is crucial to the formation of the mesoporous hollow nanostructure as well as to the homogeneous doping of Fe atoms into the CoP lattice. As revealed by experimental measurements and the DFT calculations, the doping of Fe plays a vital role in the enhancement of the

electrocatalytic activity toward water splitting by effectively regulating the adsorption energy of active species and lowering the kinetic energy barrier for water splitting. With the merits of the hollow and mesoporous structure as well as the composition and electronic modulation achieved through this synthetic strategy, the as-prepared mesoporous Fe-CoP HTPAs exhibit excellent activities toward HER and OER. To drive the current density up to 10 mA cm<sup>-2</sup>, the overpotentials of 98 and 230 mV are obtained toward HER and OER, respectively, and the cell voltage of only 1.59 V is required toward overall water splitting, which about 60 mV lower than that of CoP TPAs. We believe that the facile methodology proposed in this study can be extended to the synthesis of a variety of hollow and porous nanostructures with effective doping of heteroatoms to achieve low-cost and highly active and durable electrochemical catalysts toward water splitting.

## Supporting Information

Supporting Information is available from the Wiley Online Library or from the author.

## Acknowledgements

E.H. and J.N. contributed equally to this work. Y.H. acknowledges financial support from the Natural Science Foundation of China (21671173, 11504299), and Zhejiang Provincial Natural Science Foundation of China (LR14B010001). J.N. acknowledges the financial support from National Key Technologies R&D Program of China (2016YFA0201101), Cutting-edge Key Research Program of Chinese Academy of Sciences (QYZDB-SSW-JSC014), Natural Science Foundation of China (61674166), and Hundred Talents Program of Chinese Academy of Sciences.

## Conflict of Interest

The authors declare no conflict of interest.

## Keywords

electrocatalysis, Fe-doped CoP, hollow triangle plate arrays, overall water splitting, postsynthetic ligand exchange

Received: December 5, 2017

Revised: January 16, 2018

Published online: February 23, 2018

- [1] X. Gao, H. Zhang, Q. Li, X. Yu, Z. Hong, X. Zhang, C. Liang, Z. Lin, *Angew. Chem., Int. Ed.* **2016**, *55*, 6290; *Angew. Chem.* **2016**, *128*, 6398.
- [2] Z. Peng, D. Jia, A. M. Al-Enizi, A. A. Elzatahry, G. Zheng, *Adv. Energy Mater.* **2015**, *5*, 1402031.
- [3] Y. Jiao, Y. Zheng, M. Jaroniec, S. Z. Qiao, *Chem. Soc. Rev.* **2015**, *44*, 2060.
- [4] B. Owens-Baird, Y. V. Kolen'ko, K. Kovnir, *Chem. - Eur. J.* **2017**, <https://doi.org/10.1002/chem.201705322>.
- [5] M. Miao, J. Pan, T. He, Y. Yan, B. Y. Xia, X. Wang, *Chem. - Eur. J.* **2017**, *23*, 10947.
- [6] Y. P. Zhu, T. Y. Ma, M. Jaroniec, S. Z. Qiao, *Angew. Chem., Int. Ed.* **2017**, *56*, 1324; *Angew. Chem.* **2017**, *129*, 1344.
- [7] B. Zhang, C. Xiao, S. Xie, J. Liang, X. Chen, Y. Tang, *Chem. Mater.* **2016**, *28*, 6934.
- [8] H. Liang, A. N. Gandi, D. H. Anjum, X. Wang, U. Schwingenschlöggl, H. N. Alshareef, *Nano Lett.* **2016**, *16*, 7718.
- [9] P. Chen, T. Zhou, M. Zhang, Y. Tong, C. Zhong, N. Zhang, L. Zhang, C. Wu, Y. Xie, *Adv. Mater.* **2017**, *29*, 1701584.
- [10] H. Kaneko, T. Minegishi, K. Domen, *Chem. - Eur. J.* **2017**, <https://doi.org/10.1002/chem.201703104>.
- [11] Y. Wang, B. Kong, D. Zhao, H. Wang, C. Selomulya, *Nano Today* **2017**, *15*, 26.
- [12] D. Dai, H. Xu, L. Ge, C. Han, Y. Gao, S. Li, Y. Lu, *Appl. Catal., B* **2017**, *217*, 429.
- [13] D. Zeng, W. Xu, W. J. Ong, J. Xu, H. Ren, Y. Chen, H. Zheng, D. L. Peng, *Appl. Catal., B* **2018**, *221*, 47.
- [14] D. Zeng, W. J. Ong, H. Zheng, M. Wu, Y. Chen, D. L. Peng, M. Y. Han, *J. Mater. Chem. A* **2017**, *5*, 16171.
- [15] Z. Qin, Y. Chen, Z. Huang, J. Su, L. Guo, *J. Mater. Chem. A* **2017**, *5*, 19025.
- [16] Y. Tan, H. Wang, P. Liu, Y. Shen, C. Cheng, A. Hirata, T. Fujita, Z. Tang, M. Chen, *Energy Environ. Sci.* **2016**, *9*, 2257.
- [17] J. Li, M. Yan, X. Zhou, Z. Q. Huang, Z. Xia, C.-R. Chang, Y. Ma, Y. Qu, *Adv. Funct. Mater.* **2016**, *26*, 6785.
- [18] M. Cabán-Acevedo, M. L. Stone, J. R. Schmidt, J. G. Thomas, Q. Ding, H. C. Chang, M. L. Tsai, J. H. He, S. Jin, *Nat. Mater.* **2015**, *14*, 1245.
- [19] J. Duan, S. Chen, A. Vasileff, S. Z. Qiao, *ACS Nano* **2016**, *10*, 8738.
- [20] X. Zhang, X. Zhang, H. Xu, Z. Wu, H. Wang, Y. Liang, *Adv. Funct. Mater.* **2017**, *27*, 1606635.
- [21] B. Y. Guan, L. Yu, X. W. Lou, *Angew. Chem., Int. Ed.* **2017**, *56*, 2386; *Angew. Chem.* **2017**, *129*, 2426.
- [22] Y. Li, J. Liu, C. Chen, X. Zhang, J. Chen, *ACS Appl. Mater. Interfaces* **2017**, *9*, 5982.
- [23] P. He, X. Y. Yu, X. W. Lou, *Angew. Chem., Int. Ed.* **2017**, *56*, 3897; *Angew. Chem.* **2017**, *129*, 3955.
- [24] C. Tang, L. Gan, R. Zhang, W. Lu, X. Jiang, A. M. Asiri, X. Sun, J. Wang, L. Chen, *Nano Lett.* **2016**, *16*, 6617.
- [25] X. Xiao, C. T. He, S. Zhao, J. Li, W. Lin, Z. Yuan, Q. Zhang, S. Wang, L. Dai, D. Yu, *Energy Environ. Sci.* **2017**, *10*, 893.
- [26] Y. V. Kaneti, J. Tang, R. R. Salunkhe, X. Jiang, A. Yu, K. C. W. Wu, Y. Yamauchi, *Adv. Mater.* **2017**, *29*, 1604898.
- [27] H. Zhang, J. Nai, L. Yu, X. W. Lou, *Joule* **2017**, *1*, 77.
- [28] H. Hu, B. Y. Guan, X. W. Lou, *Chem* **2016**, *1*, 102.
- [29] H. Hu, B. Guan, B. Xia, X. W. Lou, *J. Am. Chem. Soc.* **2015**, *137*, 5590.
- [30] L. Zhang, H. B. Wu, X. W. Lou, *J. Am. Chem. Soc.* **2013**, *135*, 10664.
- [31] R. E. Morris, L. Brammer, *Chem. Soc. Rev.* **2017**, *46*, 5444.
- [32] C. K. Brozek, M. Dinca, *Chem. Soc. Rev.* **2014**, *43*, 5456.
- [33] C. Guan, W. Zhao, Y. Hu, Z. Lai, X. Li, S. Sun, H. Zhang, A. K. Cheetham, J. Wang, *Nanoscale Horiz.* **2017**, *2*, 99.
- [34] L. Yu, L. Zhang, H. B. Wu, X. W. Lou, *Angew. Chem., Int. Ed.* **2014**, *53*, 3711; *Angew. Chem.* **2014**, *126*, 3785.
- [35] J. Hao, W. Yang, Z. Zhang, J. Tang, *Nanoscale* **2015**, *7*, 11055.
- [36] G. Fang, J. Zhou, C. Liang, A. Pan, C. Zhang, Y. Tang, X. Tan, J. Liu, S. Liang, *Nano Energy* **2016**, *26*, 57.
- [37] M. S. Lin, B. I. Jan, *Electroanalysis* **1997**, *9*, 340.
- [38] E. L. Hu, J. Q. Ning, B. He, Z. Li, C. Zheng, Y. Zhong, Z. Zhang, Y. Hu, *J. Mater. Chem. A* **2017**, *5*, 2271.
- [39] T. Liu, X. Ma, D. Liu, S. Hao, G. Du, Y. Ma, A. M. Asiri, X. Sun, L. Chen, *ACS Catal.* **2017**, *7*, 98.
- [40] J. Tian, Q. Liu, A. M. Asiri, X. Sun, *J. Am. Chem. Soc.* **2014**, *136*, 7587.
- [41] S. Han, Y. Feng, F. Zhang, C. Yang, Z. Yao, W. Zhao, F. Qiu, L. Yang, Y. Yao, X. Zhuang, X. Feng, *Adv. Funct. Mater.* **2015**, *25*, 3899.

- [42] Y. Yan, B. Zhao, S. C. Yi, X. Wang, *J. Mater. Chem. A* **2016**, *4*, 13005.
- [43] L. Zhao, Q. Cao, A. Wang, J. Duan, W. Zhou, Y. Sang, H. Liu, *Nano Energy* **2018**, *45*, 118.
- [44] C. Guan, X. Liu, A. M. Elshahawy, H. Zhang, H. Wu, S. J. Pennycook, J. Wang, *Nanoscale Horiz.* **2017**, *2*, 342.
- [45] J. Zhang, T. Wang, D. Pohl, B. Rellinghaus, R. Dong, S. Liu, X. Zhuang, X. Feng, *Angew. Chem., Int. Ed.* **2016**, *55*, 6702; *Angew. Chem.* **2016**, *128*, 6814.
- [46] Y. H. Chang, F. Y. Wu, T. Y. Chen, C. L. Hsu, C. H. Chen, F. Wiryo, K. H. Wei, C. Y. Chiang, L. J. Li, *Small* **2014**, *10*, 895.
- [47] C. G. Morales-Guio, L. Liardet, X. Hu, *J. Am. Chem. Soc.* **2016**, *138*, 8946.
- [48] J. Duan, S. Chen, C. Zhao, *Nat. Commun.* **2017**, *8*, 15341.
- [49] M. Govindhan, B. Mao, A. Chen, *Nanoscale* **2016**, *8*, 1485.
- [50] M. S. Burke, M. G. Kast, L. Trotochaud, A. M. Smith, S. W. Boettcher, *J. Am. Chem. Soc.* **2015**, *137*, 3638.
- [51] K. Liu, C. Zhang, Y. Sun, G. Zhang, X. Shen, F. Zou, H. Zhang, Z. Wu, E. C. Wegener, C. J. Taubert, J. T. Miller, Z. Peng, Y. Zhu, *ACS Nano* **2018**, *12*, 158.
- [52] M. Bajdich, M. García-Mota, A. Vojvodic, J. K. Nørskov, A. T. Bell, *J. Am. Chem. Soc.* **2013**, *135*, 13521.
- [53] A. Mendoza-Garcia, H. Zhu, Y. Yu, Q. Li, L. Zhou, D. Su, M. J. Kramer, S. Sun, *Angew. Chem., Int. Ed.* **2015**, *54*, 9642; *Angew. Chem.* **2015**, *127*, 9778.
- [54] D. Friebel, M. W. Louie, M. Bajdich, K. E. Sanwald, Y. Cai, A. M. Wise, M. J. Cheng, D. Sokaras, T. C. Weng, R. Alonso-Mori, R. C. Davis, J. R. Bargar, J. K. Nørskov, A. Nilsson, A. T. Bell, *J. Am. Chem. Soc.* **2015**, *137*, 1305.